

Geophysical Research Letters[®]



RESEARCH LETTER

10.1029/2021GL097013

Key Points:

- The phase velocity and wavelength of coexisting ionospheric cusp density and electric field fluctuations is determined using interferometry
- In-situ confirmation of decameter–meter-scale density and electric field fluctuations having low phase velocity in the plasma frame
- Intermittent decameter-scale fluctuations coincide with larger-scale density variations outside of enhanced precipitation regions

Correspondence to:
















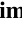

A. Spicher,
andres.spicher@uit.no

Citation:

Spicher, A., LaBelle, J., Bonnell, J. W., Roglans, R., Moser, C., Fuselier, S. A., et al. (2022). Interferometric study of ionospheric plasma irregularities in regions of phase scintillations and HF backscatter. *Geophysical Research Letters*, 49, e2021GL097013. <https://doi.org/10.1029/2021GL097013>

Received 12 NOV 2021
Accepted 2 JUN 2022

Interferometric Study of Ionospheric Plasma Irregularities in Regions of Phase Scintillations and HF Backscatter

Andres Spicher¹ , James LaBelle² , John W. Bonnell³ , Roger Roglans³, Chrystal Moser² , Stephen A. Fuselier^{4,5} , Scott Bounds⁶ , Lasse B. N. Clausen⁷ , Francesca Di Mare⁷ , Connor A. Feltman⁶ , Yaqi Jin⁷ , Craig Kletzing⁶ , Wojciech J. Miloch⁷ , Jøran I. Moen^{7,8} , Kjellmar Oksavik^{8,9} , Rhyan Sawyer^{4,5} , Toru Takahashi^{7,10} , and Tim K. Yeoman¹¹ 

¹Department of Physics and Technology, UIT the Arctic University of Norway, Tromsø, Norway, ²Department of Physics and Astronomy, Dartmouth College, Hanover, NH, USA, ³Space Sciences Laboratory, University of California Berkeley, Berkeley, CA, USA, ⁴Southwest Research Institute, San Antonio, TX, USA, ⁵Department of Physics and Astronomy, University of Texas at San Antonio, San Antonio, TX, USA, ⁶University of Iowa, Iowa City, IA, USA, ⁷Department of Physics, University of Oslo, Oslo, Norway, ⁸University Centre in Svalbard, Longyearbyen, Norway, ⁹Birkeland Centre for Space Science, Department of Physics and Technology, University of Bergen, Bergen, Norway, ¹⁰Electronic Navigation Research Institute, National Institute of Maritime, Port, and Aviation Technology, Tokyo, Japan, ¹¹Physics and Astronomy, University of Leicester, Leicester, UK

Abstract We investigate the nature of small-scale irregularities observed in the cusp by the Twin Rockets to Investigate Cusp Electrodynamics-2 (TRICE-2) in regions of enhanced phase scintillations and high-frequency coherent radar backscatter. We take advantage of the fact that the irregularities were detected by spatially separated probes, and present an interferometric analysis of both the observed electron density and electric field fluctuations. We provide evidence that fluctuations spanning a few decameters to about a meter have low phase velocity in the plasma reference frame and are nondispersive, confirming that decameter-scale irregularities follow the $\mathbf{E} \times \mathbf{B}$ velocity. Furthermore, we show that these “spatial” structures are intermittent and prominent outside of regions with strongest precipitation. The observations are then discussed in the context of possible mechanisms for irregularity creation.

Plain Language Summary Ionospheric plasma are known to be highly irregular, with fluctuations evolving both in space and time. Irregular structures can reach hundreds of kilometers to a few meters and, despite being common and having space weather impacts, the details of their source(s) and behavior are still unclear, especially at smaller scales. In this work, we investigate small-scale plasma density and electric field fluctuations observed by a sounding rocket where ground-based instruments also detected irregularities. To circumvent ambiguities of interpreting measurements made by single probes, we take advantage of the fact that the fluctuations were detected by spatially separated probes and use multi-point analysis techniques to separate the spatial and temporal scales of the observed structures. The analysis allows to estimate the phase velocities and wavelengths of the fluctuations and reveals spatial irregularities from tens of meters to a meter, that is, irregularities that are slow in the plasma frame. Additionally, we show that these small-scale structures are concentrated outside of regions where most electrons are precipitating downward along the Earth's magnetic field and discuss the observations in the context of irregularity creation. Altogether, this study provides new insights into the sources and behavior of high-latitude ionospheric irregularities.

1. Introduction

Turbulent flows generally exhibit spatio-temporal randomness or an “irregularity” character spanning a wide range of scales (Tennekes et al., 1972; Tsinober, 2009). In the ionosphere, such irregular structures are common (Kelley, 2009), and meso- to small-scale fluctuations in electron density (N_e) are of particular interest for space weather. Indeed, N_e fluctuations of the order of hundreds of meters to a few kilometers can affect Global Navigation Satellite Systems signals and cause “scintillations” (rapid fluctuations in signal amplitude or phase) (Hey et al., 1946; Kintner et al., 2007; Yeh & Liu, 1982). Furthermore, decameter-scale structures cause high frequency (HF) backscatter detected by the Super Dual Auroral Radar Network (SuperDARN) (Greenwald et al., 1995).

© 2022. The Authors.
This is an open access article under the terms of the [Creative Commons Attribution License](https://creativecommons.org/licenses/by/4.0/), which permits use, distribution and reproduction in any medium, provided the original work is properly cited.

With increasing need for reliable Arctic communication and navigation systems, a detailed understanding of these irregular structures and their cause(s) is essential (e.g., Moen et al., 2013).

Of particular interest are the ionospheric cusp regions, where irregularities and phase scintillations peak (Heppner et al., 1993; Jin et al., 2015, 2019), and where SuperDARN echoes have wide and complex Doppler spectra (Baker et al., 1995; Moen et al., 2002; Villain et al., 2002). Processes such as the gradient-drift instability (GDI) (Tsunoda, 1988), particle precipitation (Dyson & Winningham, 1974; Moen et al., 2002; Ponomarenko et al., 2007), and inhomogeneous flows (Basu et al., 1994; Heppner et al., 1993; Spicher et al., 2020) are considered important. However, the dominant mechanism(s) are not yet assessed (e.g., Chisham et al., 2007; Moen et al., 2013; Ponomarenko & Waters, 2006).

To advance our understanding, it is essential to characterize properties of the fluctuations involved (e.g., Kintner & Seyler, 1985; LaBelle & Kintner, 1989). In this study, we investigate the nature of irregularities detected in the cusp by TRICE-2. While the interpretation of turbulence observations by single probes on moving spacecraft requires a priori assumptions about the fluctuations (Fredricks & Coroniti, 1976; Temerin, 1978), we take advantage of the fact that irregularities were detected by spatially separated probes. We present interferometric analysis of co-existing N_e and electric field (E -field) fluctuations observed within regions of enhanced phase scintillations and wide SuperDARN spectra, and estimate their phase velocities and corresponding wavelength. Our analysis shows the first in-situ experimental evidence of such decameter-scale irregularities (reaching scales shorter than the oxygen gyroradius) being “frozen in” in the cusp F region, an assumption essential for SuperDARN convection maps. The observations are then discussed in the context of possible mechanisms for irregularity creation.

2. Instrumentation

TRICE-2 was part of the Grand Challenge Initiative Cusp and consisted of two sounding rockets launched from Andøya, Norway, on 08 December 2018: a high-flyer (T2-H) reaching an apogee of $\sim 1,042$ km, and a low-flyer (T2-L) reaching ~ 757 km altitude. We focus here on the multi-needle Langmuir probe (mNLP) system (Bekkeng et al., 2010; Jacobsen et al., 2010) and the E -field instrument. For more information about TRICE-2, see Moser et al. (2021) and Sawyer et al. (2021).

The mNLP system consisted of four cylindrical Langmuir probes with diameter of 0.51 mm and length of 39 mm. Fixed bias voltages (3, 4.5, 6, 7.5 V) were applied to the probes, allowing N_e determination at a cadence of 10 kHz (Clausen, 2022). The interferometry analysis presented below relies on probes mNLP2 (4.5 V) and mNLP3 (6 V) located on opposite sides of the payload and separated by $d = 1$ m. Results using other probe pairs generally agree. For N_e calculations, the spin frequency and two harmonics were removed using band-pass filters (Jacobsen et al., 2010), and it was assumed that the probes did not act as infinitely long cylinders (assumptions: $\beta = 0.8$ and temperature $T_e = 3500$ K, see Hoang et al. (2018); Marholm and Marchand (2020)).

The DC E -field instrument consisted of four spherical probes mounted $d = 6.5$ m apart on booms deployed perpendicular to the payload axis. With this configuration the probe to probe E -field and the probe to payload potential ($\Delta\Phi$) were determined at a cadence of 2.5 kHz.

Data from ground-based instruments provide geophysical context. We show the 630 nm auroral emission obtained from an all-sky imager located in Ny-Ålesund, Norway, as well as phase scintillations indices (Fremouw et al., 1978) calculated using 1 s raw carrier phase data obtained from four receivers on Svalbard (Oksavik, 2020a, 2020b). The 1 s index ($\sigma_{\phi_{1s}}$) is calculated using a sixth-order Butterworth high-pass filter with conventional 0.1 Hz cut-off frequency (Van Dierendonck et al., 1993). To minimize errors, data with elevation angle $>25^\circ$ are used (Jin et al., 2015). We also show spectral width data from the SuperDARN (Chisham et al., 2007; Greenwald et al., 1995) radar at Hankasalmi, Finland. These data use the range-finding algorithm with corrections for 1.5 hop ionospheric backscatter (Yeoman et al., 2008, 2012).

3. Background Observations

Context is provided in Figure 1. Figures 1a and 1b show 630 nm emissions at $t = 08:38$ UT and $t = 08:40$ UT, as well as $\sigma_{\phi_{1s}} \geq 0.25$ rad calculated for $t \pm 1$ min. The latter is displayed as large and small circles for strong ($\sigma_{\phi_{1s}} \geq 0.4$ rad) and medium ($0.25 \leq \sigma_{\phi_{1s}} < 0.4$ rad) indices, respectively, with circle centers corresponding to the

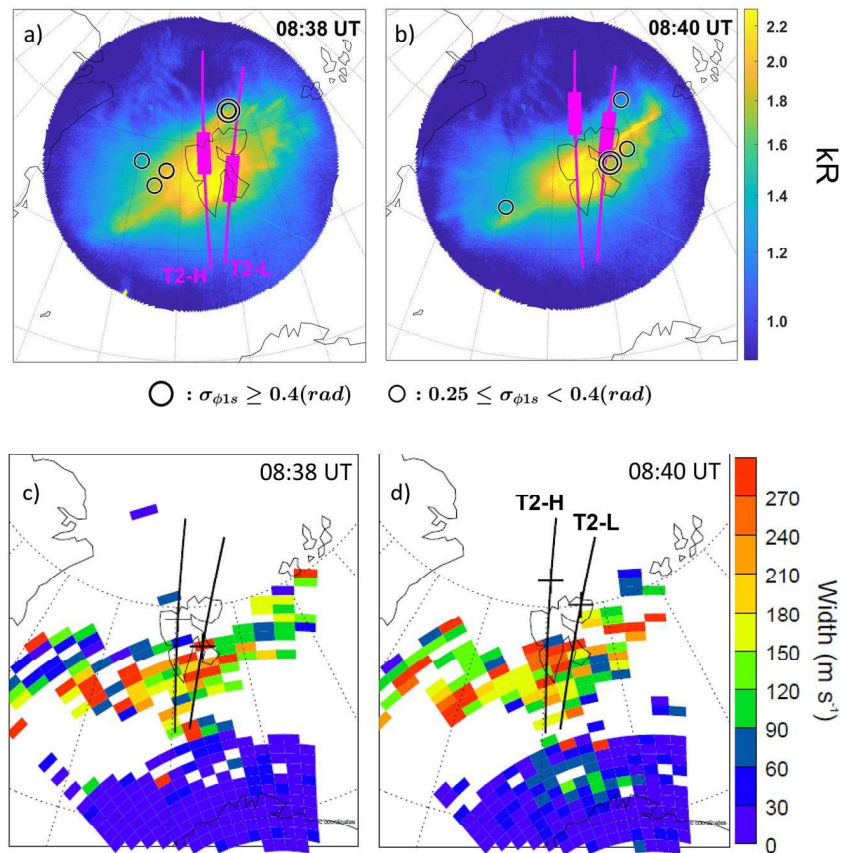


Figure 1. (a and b) 630 nm All-Sky imager data projected to 250 km altitude at $t = 08:38$ UT and $t = 08:40$ UT (color-coded) and enhanced 1 s phase scintillation indices (black circles) during $t \pm 1$ min. Payload trajectories (T2-H: high-flyer, T2-L: low-flyer) are shown in magenta, with thicker lines for $t \pm 1$ min. (c and d) Super Dual Auroral Radar Network spectral width with trajectories (black lines) and payload location (black crosses).

pierce point projected at 350 km altitude. Parts of the payload trajectories are shown using magenta lines with the thicker portions corresponding to the payload locations during $t \pm 1$ min.

Both payloads were launched into active dayside aurora. Enhanced $\sigma_{\phi 1s}$, suggesting the presence of N_e irregularities ranging from a few kilometers to hundreds of meters (Jin et al., 2017; Kintner et al., 2007), occurred on the edges of the strongest aurora, especially close to T2-L. Consequently, we focus here on observations from T2-L.

Figures 1c and 1d shows SuperDARN spectral width with the TRICE-2 trajectories superimposed. The payloads intersected regions of large spectral width. Coherent scattering from SuperDARN is expected when irregularities have wavelength (λ) matching half of the radar wavelength (Ponomarenko et al., 2007; Vallières et al., 2003), which for the current observations corresponds to $\lambda \approx 15$ m. Combining ground-based observations, we expect T2-L to observe density structures ranging from several km to $\lambda \approx 15$ m.

Figure 2 shows data from T2-L with respect to preliminary time of flight and latitude between 752 and 770 s (08:40:32–08:40:50 UT), that is, when T2-L was located in the region with the large $\sigma_{\phi 1s}$ on the poleward side of the aurora (northernmost circles in Figures 1a and 1b). Figure 2a shows N_e and the altitude of the payload. A large-scale density decrease with strong fluctuations occurs along the trajectory. These fluctuations reach frequencies >1 kHz, as seen from their wavelet power spectral density (wPSD) (Torrence & Compo, 1998) in Figures 2b. Figure 2c shows the eastward (E_E) and northward (E_N) components of the E -field. A channel of enhanced E_N is observed between 760 and 763 s, roughly in the center of the N_e fluctuations. Additionally, shorter time-scale E -field fluctuations are observed. These coincide with steep density variations/cavities and exhibit enhanced irregularity power at a few hundred Hz. This is better seen in Figure 2d showing the wPSD of ΔE_E . Sun

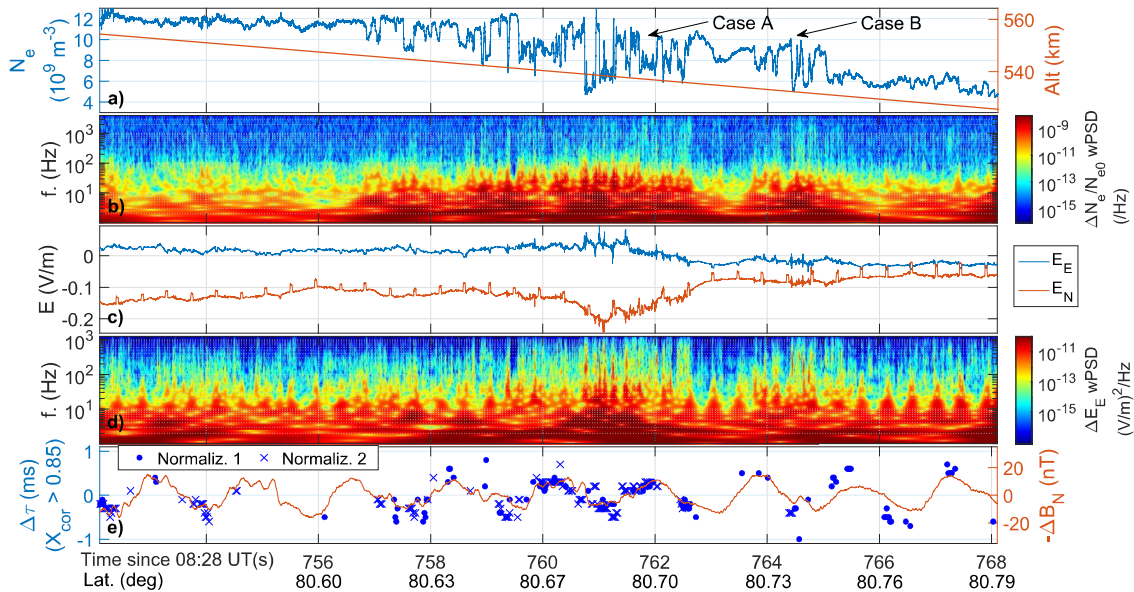


Figure 2. (a) N_e and payload altitude. (b) Wavelet spectrogram of N_e fluctuations. (c) Eastward (E_E) and Northward (E_N) components of the E -field. Periodic spikes occur when an antenna probe enters the rocket's shadow. (d) Wavelet spectrogram of ΔE_E . (e) Time shifts $\Delta\tau$ of maximum cross-correlation between currents fluctuations measured by two multi-needle Langmuir probes. The red curve exhibits (median-filtered) magnetic field fluctuations reflecting the payload spin.

spikes and possibly short wavelengths attenuation effects may contribute to the periodic modulations of broadband E -field data visible in Figure 2d.

Figures 2b and 2d show the presence of N_e and E -field fluctuations reaching >1 kHz, with enhancements in irregularity power at a few hundred Hertz close to large N_e -variations. While measured in the time-domain, in the following, we use the fact that fluctuations were measured by spatially separated probes to assess their phase velocity and corresponding wavelengths.

4. Interferometry Analysis of Density and Electric Field Fluctuations

4.1. Cross-Correlation

The phase velocity and wavelengths of N_e and E -field fluctuations along a rocket-borne interferometer axis are calculated from the cross-correlation function (X_{cor}) (LaBelle et al., 1986; Pécseli et al., 1989). We computed X_{cor} for normalized current fluctuations measured by mNLP2 and mNLP3 over intervals of 0.1 s, which is much shorter than the payload spin period of about 1.78 s. Figure 2e shows the non-zero time delays $\Delta\tau$ of maximum X_{cor} for current fluctuations that are significantly correlated. Results using two different current normalization are shown: by removing the mean (Normaliz. 1) and a cubic spline (Normaliz. 2).

$\Delta\tau$ follows a periodic pattern consistent with the payload spin, as seen from variations in the measured magnetic field (minus its mean value) at the spin period (ΔB_N in Figure 2e). This pattern means that mNLP2 observes the fluctuations before mNLP3 during half a rotation, and vice-versa during the second half of the rotation. This sequencing is consistent with the response expected for two probes spinning in field-aligned structures propagating from one direction perpendicular to the payload axis (LaBelle et al., 1986). From $\Delta\tau$ and the probe separation, one can estimate the apparent velocity v_ϕ along the interferometer axis (LaBelle et al., 1986; Pécseli et al., 1989). For instance, Case A and B highlight features that exhibited clear small-scale density fluctuations during different spin periods. For A, $v_{E \times B} \approx 3,650$ m/s and $v_\phi \approx 3,333$ m/s, while for B, $v_{E \times B} \approx 1,900$ m/s and $v_\phi \approx 2,500$ m/s. These features are discussed below.

4.2. Cross-Spectral Density Analysis

The velocities calculated using X_{cor} are unambiguous estimates of v_ϕ if the coherent frequency components are phase-shifted proportionally for each frequency (Pécseli et al., 1989). Cross-power spectral density (CPSD)

analysis in this section provides information about the phase-shift with respect to frequencies (e.g., Kintner et al., 1984).

Four examples are shown in Figure 3, where the left and right columns correspond to features A and B, respectively. CPSDs were computed using Matlab's build-in function with a Tukey window with 50% overlap (Welch, 1967). Figures 3a and 3b show the magnitude-squared coherence of the current fluctuations (shown in inlet) and Figures 3c and 3d the corresponding phase angles θ . Coherent frequency components are shown as filled dots. θ for coherent components follows a linear trend, suggesting that the structures are nondispersive (Holmgren & Kintner, 1990). The opposite sign of the slopes for each case is again consistent with Case A and B occurring in different periods of the spin.

For CPSD of N_e fluctuations with $\lambda > d$, the wavenumber \mathbf{k} and θ can be related through $\theta(\omega) = \mathbf{k} \cdot \mathbf{d}$ (LaBelle & Kintner, 1989). Thus, for a linear dispersion relation with constant $v_\phi = \omega/k$, the velocity along the interferometer axis is given by (Bonnell et al., 1996; Holmgren & Kintner, 1990)

$$v_\phi = 2\pi d \left(\frac{d\theta}{df} \right)^{-1}. \quad (1)$$

In Figures 3c and 3d, the solid black lines exhibit θ expected from a time-shift due to $v_\phi = v_{E \times B}$, and the magenta lines result from linear fits, with corresponding velocities shown in the legend. For case A, $v_\phi \approx v_{E \times B}$, while for B, $v_\phi \approx v_{E \times B} + 500$ m/s, which is consistent with results using X_{corr} . Additionally, the wrap-arounds at $f \approx 1,750$ Hz (Case A) and $f \approx 1,250$ Hz (Case B) provide direct estimates of the wavelengths (Pfaff et al., 1997). Here, they occur for $\lambda = 2d$ and using the frequencies above-mentioned and v_ϕ from the fits, the estimated interferometric baselines are 1.1 and 0.97 m, which is close to the mNLP separation $d = 1$ m.

Figures 3e and 3f show the PSDs of mNLP fluctuations. Coherent frequencies can be converted to wavenumbers since from panels (c and d), the conversion appears linear. For A, enhanced coherent PSD is seen between $k \approx 1 \text{ m}^{-1}$ and $k \approx 3 \text{ m}^{-1}$, and for Case B, enhancement is seen around $k \approx [0.5 - 1] \text{ m}^{-1}$, that is, close to $\lambda = 15$ m (vertical dashed line). Analysis suggests the presence of irregular structures reaching λ comparable to and shorter than the cold ($T_i = 1000$ K) oxygen ion gyroradius $\rho_{O^+} \approx 2.9$ m.

Figures 3g–3i show similar analysis performed for the E -field using $\Delta\Phi_3$ and $\Delta\Phi_4$ measured on opposite sides of the payload. During the intervals shown, $\Delta\Phi$'s intersects suggest that \mathbf{d} was roughly aligned with $\mathbf{v}_{E \times B}$. The time intervals are offset by about 0.2 s compared to N_e intervals (rotation of $\sim 45^\circ$) since the instruments were not aligned. As for N_e , the relation between θ and the frequencies is linear with opposite slope signs for each case, but with origins shifted by π . This is consistent with the response expected from an E -field perturbation where θ and \mathbf{k} are related through $\theta(\omega) = \frac{\mathbf{k} \cdot \mathbf{d}}{2} + \pi$ (Kintner et al., 1984; LaBelle & Kintner, 1989). Using this equation and $d/2 = 3.25$ m, v_ϕ obtained along the E -field interferometer are consistent with the ones calculated using the mNLPs. Estimated wrap-arounds at $f \approx 1,100$ Hz (Case A) $f \approx 750$ Hz (Case B) confirm the baseline of $\lambda = d/2 = 3.25$ m. Furthermore, for both cases shown, enhanced coherent PSD is seen in the range $k \approx [0.2 - 1.5] \text{ m}^{-1}$ with maxima close to $k \approx 0.5 \text{ m}^{-1}$ or $\lambda = 15$ m.

The CPSDs shown in Figure 3 suggest that the fluctuations have low phase velocity in the plasma. Such irregularities have been termed “spatial irregularities” (e.g., Holmgren & Kintner, 1990; Kintner et al., 1987; Stasiewicz & Khotyaintsev, 2001). To investigate a larger part of the flight, the procedure was automated for the 500–780 s interval. CPSDs were computed every 0.02 s using the same method as for Figure 3. For each CPSD, a linear regression was fitted to θ for $f = [150, 1,000]$ Hz (mNLP) and $f = [100, 600]$ Hz ($\Delta\Phi$) (based on Figure 3 and testing). v_ϕ was calculated for θ s exhibiting reasonably linear trends, that is, fits with more than 20 variables and an adjusted coefficient of determination $R^2 > 0.7$ (mNLP) and $R^2 > 0.9$ ($\Delta\Phi$). Structures are highly intermittent and these adjustable parameters (length of interval, frequency range, goodness of fit, threshold for fluctuations being “coherent,” etc.), as well as an unknown exact angle between the interferometer baselines and the structures give rise to uncertainties in the velocity calculations: as seen in Figure 3, significant spread in θ exist, and automatized fits may not always capture the trend adequately. Further developing robust interferometric methods is however left for future work.

Results are presented in Figure 4. Panel (a) shows N_e and the eastward component of the magnetic field (B_{East}). Positive slopes in B_{East} are expected to correspond to downward currents (Lühr et al., 1996). Figure 4b shows v_ϕ

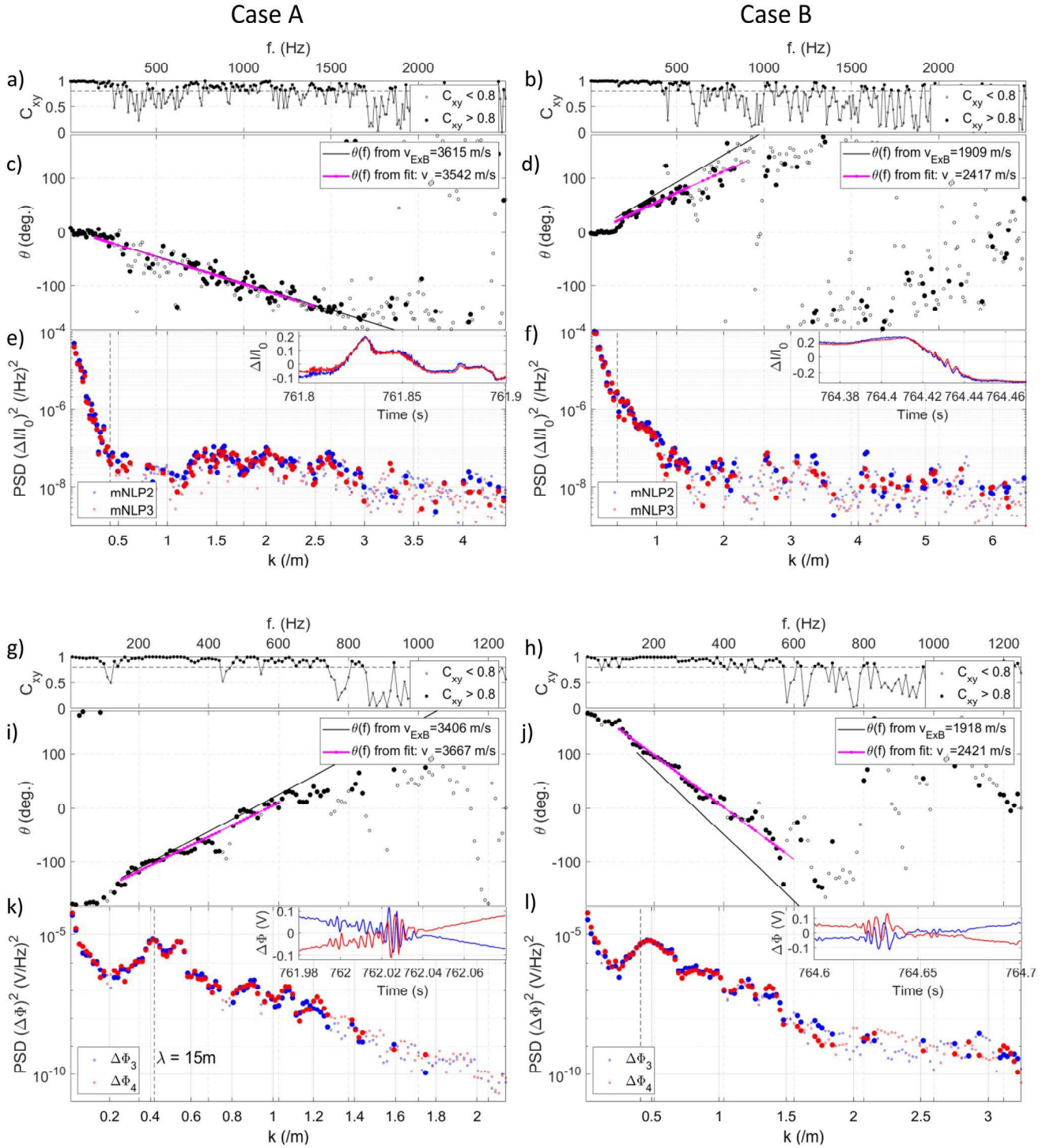


Figure 3. (a and b) Magnitude squared coherence (C_{xy}) of relative multi-needle Langmuir probe current fluctuations. (c and d) Relative phase angles θ of the current fluctuations. The black and magenta lines show θ obtained assuming Doppler shift due to v_{ExB} and from a fit, respectively. (e and f) PSD of the current fluctuations. (g–l) Similar analysis for the E -field. Filled dots are used for frequency components with $C_{xy} > 0.8$.

with confidence intervals ($\pm 2\sigma$ on the regression coefficients) obtained from the automated method applied to mNLP (magenta) and different E -field probe pairs (blue/cyan). The black line shows v_{ExB} . Calculated v_{ϕ} s are relatively noisy and it is easier to obtain linearity for the E -field probes; however, values appear generally consistent with v_{ExB} suggesting low phase velocities in the plasma. Most of the structures with θ exhibiting linear trends for

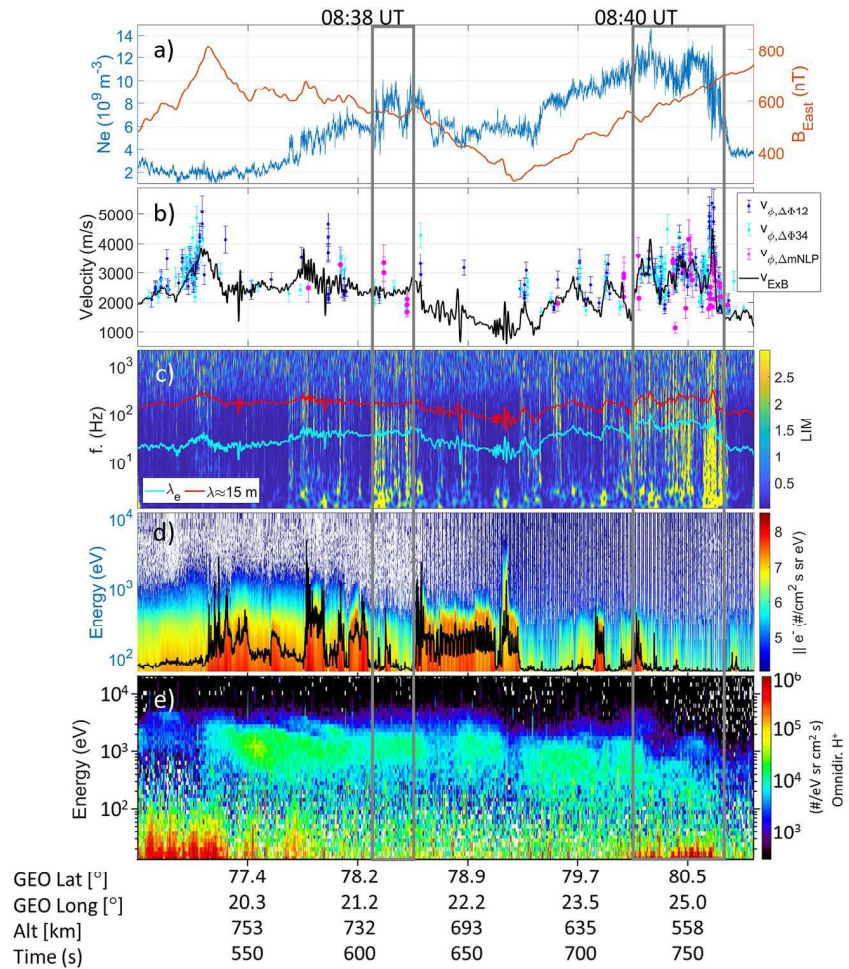


Figure 4. (a) N_e and B_{East} . (b) Velocities obtained using Cross-spectral density analysis on multi-needle Langmuir probe (magenta) and E -field (blue/cyan) data for different probe pairs. (c) Local intermittency Analysis of mNLP3 current with the electron inertial length λ_e and $\lambda \approx 15$ m superimposed. (d) Electron number flux parallel to \mathbf{B} (color) and total number flux (black line, a.u.). (e) Omnidirectional ion number flux. Times from Figure 1 are annotated at the top.

both N_e and E are clustered between about 725 and 765 s. Significant E -field and some sparse N_e fluctuations are also observed at other times, for example, at about 505–530 s and around 610 s.

To investigate N_e inhomogeneities, we applied Local Intermittency Analysis (LIM), which accentuates times and frequencies at which the power is intensified compared to the average power in the fluctuations (Farge, 1992; Tam et al., 2005). The LIM was calculated using Morlet wavelets (Torrence & Compo, 1998), and results for mNLP3 are shown in Figure 4c. Several intervals with significant LIM are observed, with the most prominent highlighted with the gray boxes and encompassing where most nondispersive N_e irregularities are detected. For these, frequencies can be translated to wavelengths (Holmgren & Kintner, 1990) and, to guide the eye, the electron inertial length λ_e and the characteristic $\lambda \approx 15$ m for SuperDARN backscatter are shown. Several intervals exhibit intermittent structures with $\lambda < \lambda_e$ and $\lambda \leq 15$ m.

Panels (d and e) exhibit the parallel ($\pm 10^\circ$ with respect to \mathbf{B}) electron and omnidirectional ion number fluxes, respectively. Most electron precipitation has energies below 1 keV, as expected for cusp aurora (e.g., Vontrat-Reberac et al., 2001). In panel (d), the number flux sum is also shown as a black line for visualization purposes. From Figure 4, it appears that most spatial and nondispersive small-scale irregularities are detected outside of regions with the strongest precipitation, and within intervals where B_{East} has roughly positive slope. Also, many of the 15 m N_e irregularities coincide with ion upflows around 720–760 s (pitch angle of about 135° , not shown).

5. Summary and Interpretation

This work presents a detailed investigation of N_e and E -field fluctuations in the polar ionosphere. While interpreting in-situ “single-point” observations of irregularities and turbulence is generally ambiguous (Fredricks & Coroniti, 1976; Guio & Pécseli, 2021; Temerin, 1978), interferometry techniques separate the spatial and temporal scales of F region irregularities in the cusp. The analysis revealed nondispersive irregularities with low phase velocity in the plasma frame, allowing to estimate irregularity power in wavenumber domain, which is essential to interpret observations with respect to turbulence theories (Kintner & Seyler, 1985). Analysis shows the presence of enhanced spatial oscillations around $k \sim 0.5 \text{ m}^{-1}$, that is, close to the characteristic $\lambda = 15 \text{ m}$ for SuperDARN backscatter, as well as extending down to $k\rho_{O^+} \geq 1$. This provides in-situ confirmation of decameter-scale N_e irregularities moving with the $\mathbf{E} \times \mathbf{B}$, an essential hypothesis to derive line-of-sight velocities from HF radars and large-scale convection patterns from SuperDARN (e.g., Makarevich & Bristow, 2014; Ruohoniemi et al., 1989, 1987; Villain et al., 1985).

This study supplements previous detection of spatial irregularities, see reviews by LaBelle et al. (1986) and Temerin and Kintner (1989) and references therein. In the upper polar ionosphere, examples include E -field inhomogeneities detected by Kelley and Mozer (1972) and zero-frequency turbulence commonly identified from “fingerprint” patterns (for $\lambda < d$) (Temerin, 1978, 1979). Also, cusp E -field waves above 5,700 km have been shown to have low v_ϕ (Angelopoulos et al., 2001). For N_e , spatial irregularities were frequently observed at higher altitudes using satellites (Holmgren & Kintner, 1990; Kintner et al., 1987; Reiniusson et al., 2006; Stasiewicz & Gustafsson, 2000; Stasiewicz et al., 2000); however, our high-resolution observations of coinciding N_e and E -field fluctuations for which the phase velocities (and consequently wavenumbers/wavelengths) could be assessed are unique, especially in the cusp F region where scintillations and wide HF spectra are also observed.

Decameter-scale E -field and N_e fluctuations are identified and velocities obtained for both quantities are consistent, suggesting they are locked. Poleward of the aurora (Figure 2), they coincide with larger-scale (hundreds of meters) steep N_e -variations, suggesting they result as secondary processes (Moen et al., 2012). 10-m F region N_e structures have previously been suggested to spawn down from km-scale gradients (Moen et al., 2012; Spicher et al., 2014) and, for T2-L, observations of intermittent fluctuations at specific wavenumber ranges are shown (especially clear for E -field). Drift-waves (e.g., Pécseli, 2015) and GDI can be excited on density gradients. GDI is often regarded as dominant in the F region (Lamarche et al., 2020; Tsunoda, 1988) and can indeed cause decameter-scale structures directly, provided favorable conditions exist (Makarevich, 2017). While the flow was dominantly perpendicular to the rocket motion, the $\sim 11 \text{ m}$ structures seen in Figure 3f) may result from GDI on the larger-scale N_e -variation since $v_{E \times B}$ exhibited a southward component (anti-parallel to the along-track variation). In fact, Makarevich (2017) showed that, for strong convection in the F region, the most favorable conditions for GDI occurred when ∇N_e and $v_{E \times B}$ are not exactly aligned. Observations of decameter-scale structures on N_e -variations with opposite signs when the flow exhibited a northward component (not shown) further support GDI. Moreover, linear kinetic theory also suggests GDI grows at $k\rho_i > 1$ for typical ionospheric conditions for large $v_{E \times B}$, but additional theoretical developments are needed (Gary & Cole, 1983), also to assess the E -field oscillations at $k \approx 0.5 \text{ m}^{-1}$. Note that our cusp observations of intermittent fluctuations are in line with findings from Tam et al. (2005), who showed the presence of highly intermittent E -field fluctuations lasting a few milliseconds in the auroral oval. Tam et al. (2005) suggested this to be indications that broadband extremely low frequency fluctuations were caused by sporadic and localized coherent structures interacting nonlinearly (Chang, 2001).

Not all small-scale N_e fluctuations were co-located with larger-scale N_e -variations (see Figure 3e) and other mechanisms were likely at play during the flight. Particle precipitation is believed to be important at high latitudes and for HF backscatter (e.g., Dyson & Winningham, 1974; Moen et al., 2002; Ponomarenko et al., 2007). Here, the largest occurrence of N_e irregularities was detected poleward of the cusp, adjacent to regions with intense electron fluxes. Precipitation was thus unlikely a dominant direct driver of decameter-scale structures, but it may have caused “seed” irregularities for secondary processes (Moen et al., 2012; Oksavik et al., 2012).

As seen in Figure 2c, a flow shear was observed at about 762 s. The shear scale-size matches that used in numerical simulations showing that KHI could quickly cause irregularities at scintillation scales in the cusp (Spicher et al., 2020). However, KHI is mostly a long-wavelength, low-frequency, instability and therefore it fails to explain direct creation of $k\rho_{O^+} \geq 1$ structures (Ganguli et al., 1994). Secondary processes such as the inhomogeneous

energy density driven instability (Ganguli et al., 1985) could operate; however, the shear frequency (~ 1 Hz) is low compared to the O^+ gyrofrequency (~ 40 Hz), suggesting that this instability is not dominant (Ganguli et al., 1994).

Alternatively, the coincidence between positive slopes in B_{East} ion upflows and the largest concentration of spatial structures is intriguing. Upper F region N_e enhancements and the presence of larger-scale fluctuations in the return current (as seen poleward of the cusp in Figure 4) are consistent with simulations and observations associated with the ionospheric Alfvén resonator (Cohen et al., 2013; Streltsov & Lotko, 2008). Especially, dispersive Alfvén waves (Stasiewicz et al., 2000) and electrostatic slow ion cyclotron/acoustic waves (for hot ions) have been suggested as processes with low phase velocity and broadband low-frequency E -field fluctuations (Seyler & Wahlund, 1996; Seyler et al., 1998; Wahlund et al., 1998). Altogether, this study provides new insights into the behavior of small-scales N_e and E -field irregularities as well as physical context for what causes wide SuperDARN spectra in the cusp, and further analysis will hopefully help resolve the exact mechanism(s) taking place.

Data Availability Statement

Data from the TRICE-2 missions can be found at: https://phi.physics.uiowa.edu/science/tau/data0/rocket/SCIENCE/TRICEII_Mission/. mNLP data is available at <https://archive.sigma2.no/pages/public/dataset-Detail.jsf?id=10.11582/2022.00032> (Clausen, 2022). Super Dual Auroral Radar Network data is available at <https://www.frd-r-dfdr.ca/repo/collection/superdarn> with basic data analysis software at <https://zenodo.org/record/4435297>. The imager data are available at <http://tid.uio.no/plasma/aurora/>. The wavelet analysis is based on an adapted version of a (Morlet) wavelet software provided by C. Torrence and G. Compo (Torrence & Compo, 1998, latest version is available at URL: <http://atoc.colorado.edu/research/wavelets/>). The panel showing ion data was obtained using SPEDAS V3.2 (Angelopoulos et al., 2019).

Acknowledgments

The multi-needle Langmuir probe (mNLP) and University of Oslo (UiO) participation in the GCI Cusp campaign were funded through the Research Council of Norway (RCN) Grant 275653. A. Spicher (Grant 326039), Y. Jin and L. B. N. Clausen (Grant 235655), and K. Oksavik (Grant 223252) acknowledge funding from RCN. T. K. Yeoman was supported by STFC Grant ST/S000429/1. T. Takahashi was supported by JSPS Overseas Research Fellowships and KAKENHI Grant No. JP20K14544. Research at Southwest Research Institute was funded through the NASA TRICE-2 mission grant NNX15AL08G. This study was initiated within the 4D Space research group, and supported in part by the European Research Council under the European Union's Horizon 2020 research and innovation programme (Grant 866357). The ASI are supported by RCN contract 230935. The authors acknowledge the use of Super Dual Auroral Radar Network (SuperDARN) data. SuperDARN is a collection of radars funded by national scientific funding agencies of Australia, Canada, China, France, Italy, Japan, Norway, South Africa, United Kingdom, and the United States of America. The authors thank Espen Trondsen, David Bang-Hauge, and the UiO Mechanical Workshop for the mNLP, Christopher Ivar for ephemeris data, Andøya Space for launch operations, KHO/UNIS/UiO for ground-based support, everyone involved in the missions, and the referees for helping improving the manuscript.

References

- Angelopoulos, V., Cruce, P., Drozdov, A., Grimes, E., Hatzigeorgiu, N., King, D., et al. (2019). The space physics environment data analysis system (SPEDAS). *Space Science Reviews*, 215(1), 9. <https://doi.org/10.1007/s11214-018-0576-4>
- Angelopoulos, V., Mozer, F. S., Bonnell, J., Temerin, M., Somoza, M., Peterson, W. K., et al. (2001). Wave power studies of cusp crossings with the Polar satellite. *Journal of Geophysical Research*, 106(A4), 5987–6006. <https://doi.org/10.1029/2000JA900127>
- Baker, K. B., Dudency, J. R., Greenwald, R. A., Pinnock, M., Newell, P. T., Rodger, A. S., et al. (1995). HF radar signatures of the cusp and low-latitude boundary layer. *Journal of Geophysical Research*, 100(A5), 7671–7695. <https://doi.org/10.1029/94JA01481>
- Basu, S., Basu, S., Chaturvedi, P. K., & Bryant, C. M., Jr. (1994). Irregularity structures in the cusp/cleft and polar cap regions. *Radio Science*, 29(1), 195–207. <https://doi.org/10.1029/93RS01515>
- Bekkeng, T. A., Jacobsen, K. S., Bekkeng, J. K., Pedersen, A., Lindem, T., Lebreton, J.-P., & Moen, J. I. (2010). Design of a multi-needle Langmuir probe system. *Measurement Science and Technology*, 21(8), 085903. <https://doi.org/10.1088/0957-0233/21/8/085903>
- Bonnell, J., Kintner, P., Wahlund, J.-E., Lynch, K., & Arnoldy, R. (1996). Interferometric determination of broadband ELF wave phase velocity within a region of transverse auroral ion acceleration. *Geophysical Research Letters*, 23(23), 3297–3300. <https://doi.org/10.1029/96GL03238>
- Chang, T. (2001). Colloid-like behavior and topological phase transitions in space plasmas: Intermittent low frequency turbulence in the auroral zone. *Physica Scripta*, T89(1), 80. <https://doi.org/10.1238/physica.topical.089a00080>
- Chisham, G., Lester, M., Milan, S. E., Freeman, M. P., Bristow, W. A., Grocott, A., et al. (2007). A decade of the Super Dual Auroral Radar Network (SuperDARN): Scientific achievements, new techniques and future directions. *Surveys in Geophysics*, 28(1), 33–109. <https://doi.org/10.1007/s10712-007-9017-8>
- Clausen, L. (2022). *Multi-Needle Langmuir probe (m-NLP) data on TRICE-2* [Data set]. Norstore. <https://doi.org/10.11582/2022.00032>
- Cohen, I. J., Lessard, M. R., Kaeppler, S. R., Bounds, S. R., Kletzing, C. A., Streltsov, A. V., et al. (2013). Auroral Current and Electrodynamics Structure (ACES) observations of ionospheric feedback in the Alfvén resonator and model responses. *Journal of Geophysical Research: Space Physics*, 118(6), 3288–3296. <https://doi.org/10.1002/jgra.50348>
- Dyson, P. L., & Winningham, J. D. (1974). Top side ionospheric spread F and particle precipitation in the day side magnetospheric clefts. *Journal of Geophysical Research*, 79(34), 5219–5230. <https://doi.org/10.1029/JA079i034p05219>
- Farge, M. (1992). Wavelet transforms and their applications to turbulence. *Annual Review of Fluid Mechanics*, 24(1), 395–458. <https://doi.org/10.1146/annurev.fl.24.010192.002143>
- Fredricks, R. W., & Coroniti, F. V. (1976). Ambiguities in the deduction of rest frame fluctuation spectrums from spectrums computed in moving frames. *Journal of Geophysical Research*, 81(31), 5591–5595. <https://doi.org/10.1029/JA081i031p05591>
- Fremouw, E. J., Leadabrand, R. L., Livingston, R. C., Cousins, M. D., Rino, C. L., Fair, B. C., & Long, R. A. (1978). Early results from the DNA Wideband satellite experiment—Complex-signal scintillation. *Radio Science*, 13(1), 167–187. <https://doi.org/10.1029/RS013i001p0167>
- Ganguli, G., Keskinen, M. J., Romero, H., Heelis, R., Moore, T., & Pollock, C. (1994). Coupling of microprocesses and macroprocesses due to velocity shear: An application to the low-altitude ionosphere. *Journal of Geophysical Research*, 99(A5), 8873–8889. <https://doi.org/10.1029/93JA03181>
- Ganguli, G., Palmadesso, P., & Lee, Y. C. (1985). A new mechanism for excitation of electrostatic ion cyclotron waves and associated perpendicular ion heating. *Geophysical Research Letters*, 12(10), 643–646. <https://doi.org/10.1029/GL012i010p00643>

- Gary, S. P., & Cole, T. E. (1983). Pedersen density drift instabilities. *Journal of Geophysical Research*, 88(A12), 10104–10110. <https://doi.org/10.1029/JA088iA12p10104>
- Greenwald, R. A., Baker, K. B., Dudeney, J. R., Pinnock, M., Jones, T. B., Thomas, E. C., et al. (1995). Darn/Superdarn: A global view of the dynamics of high-latitude convection. *Space Science Reviews*, 71(1–4), 761–796. <https://doi.org/10.1007/BF00751350>
- Guio, P., & Pécseli, H. L. (2021). The impact of turbulence on the ionosphere and magnetosphere. *Frontiers in Astronomy and Space Sciences*, 7, 107. <https://doi.org/10.3389/fspas.2020.573746>
- Heppner, J. P., Liebrecht, M. C., Maynard, N. C., & Pfaff, R. F. (1993). High-latitude distributions of plasma waves and spatial irregularities from DE 2 alternating current electric field observations. *Journal of Geophysical Research*, 98(A2), 1629–1652. <https://doi.org/10.1029/92JA01836>
- Hey, J. S., Parsons, S. J., & Phillips, J. W. (1946). Fluctuations in cosmic radiation at radio-frequencies. *Nature*, 158(4007), 234. <https://doi.org/10.1038/158234a0>
- Hoang, H., Røed, K., Bekkeng, T. A., Moen, J. I., Spicher, A., Clausen, L. B. N., et al. (2018). A study of data analysis techniques for the multi-needle Langmuir probe. *Measurement Science and Technology*, 29(6), 065906. <https://doi.org/10.1088/1361-6501/aab948>
- Holmgren, G., & Kintner, P. M. (1990). Experimental evidence of widespread regions of small-scale plasma irregularities in the magnetosphere. *Journal of Geophysical Research*, 95(A5), 6015–6023. <https://doi.org/10.1029/JA095iA05p06015>
- Jacobsen, K. S., Pedersen, A., Moen, J. I., & Bekkeng, T. A. (2010). A new Langmuir probe concept for rapid sampling of space plasma electron density. *Measurement Science and Technology*, 21(8), 085902. <https://doi.org/10.1088/0957-0233/21/8/085902>
- Jin, Y., Moen, J. I., & Miloch, W. J. (2015). On the collocation of the cusp aurora and the GPS phase scintillation: A statistical study. *Journal of Geophysical Research: Space Physics*, 120(10), 9176–9191. <https://doi.org/10.1002/2015JA021449>
- Jin, Y., Moen, J. I., Oksavik, K., Spicher, A., Clausen, L. B. N., & Miloch, W. J. (2017). GPS scintillations associated with cusp dynamics and polar cap patches. *Journal of Space Weather Space Climate*, 7, A23. <https://doi.org/10.1051/swsc/2017022>
- Jin, Y., Spicher, A., Xiong, C., Clausen, L. B. N., Kervalishvili, G., Stolle, C., & Miloch, W. J. (2019). Ionospheric plasma irregularities characterized by the Swarm satellites: Statistics at high latitudes. *Journal of Geophysical Research: Space Physics*, 124(2), 1262–1282. <https://doi.org/10.1029/2018JA026063>
- Kelley, M. C. (2009). *The Earth's ionosphere: Plasma physics and electrodynamics*. Elsevier Science.
- Kelley, M. C., & Mozer, F. S. (1972). A satellite survey of vector electric fields in the ionosphere at frequencies of 10 to 500 Hertz: 1. Isotropic, high-latitude electrostatic emissions. *Journal of Geophysical Research*, 77(22), 4158–4173. <https://doi.org/10.1029/JA077i022p04158>
- Kintner, P. M., Kelley, M. C., Holmgren, G., Koskinen, H., Gustafsson, G., & LaBelle, J. (1987). Detection of spatial density irregularities with the Viking plasma wave interferometer. *Geophysical Research Letters*, 14(4), 467–470. <https://doi.org/10.1029/GL014i004p00467>
- Kintner, P. M., LaBelle, J., Kelley, M. C., Cahill, L. J., Jr., Moore, T., & Arnoldy, R. (1984). Interferometric phase velocity measurements. *Geophysical Research Letters*, 11(1), 19–22. <https://doi.org/10.1029/GL011i001p00019>
- Kintner, P. M., Ledvina, B. M., & dePaula, E. R. (2007). GPS and ionospheric scintillations. *Space Weather*, 5(9), S09003. <https://doi.org/10.1029/2006SW000260>
- Kintner, P. M., & Scyler, C. E. (1985). The status of observations and theory of high latitude ionospheric and magnetospheric plasma turbulence. *Space Science Reviews*, 41(1), 91–129. <https://doi.org/10.1007/BF00241347>
- LaBelle, J., & Kintner, P. M. (1989). The measurement of wavelength in space plasmas. *Reviews of Geophysics*, 27(4), 495–518. <https://doi.org/10.1029/RG027i004p00495>
- LaBelle, J., Kintner, P., & Kelley, M. (1986). Interferometric phase velocity measurements in the auroral electrojet. *Planetary and Space Science*, 34(12), 1285–1297. [https://doi.org/10.1016/0032-0633\(86\)90065-6](https://doi.org/10.1016/0032-0633(86)90065-6)
- Lamarque, L. J., Varney, R. H., & Siefring, C. L. (2020). Analysis of plasma irregularities on a range of scintillation-scales using the resolute bay incoherent scatter radars. *Journal of Geophysical Research: Space Physics*, 125(3), e2019JA027112. <https://doi.org/10.1029/2019JA027112>
- Lühr, H., Warnecke, J. F., & Rother, M. K. A. (1996). An algorithm for estimating field-aligned currents from single spacecraft magnetic field measurements: A diagnostic tool applied to Freja satellite data. *IEEE Transactions on Geoscience and Remote Sensing*, 34(6), 1369–1376. <https://doi.org/10.1109/36.544560>
- Makarevich, R. A. (2017). Critical density gradients for small-scale plasma irregularity generation in the E and F regions. *Journal of Geophysical Research: Space Physics*, 122(9), 9588–9602. <https://doi.org/10.1002/2017JA024393>
- Makarevich, R. A., & Bristow, W. A. (2014). Coordinated radar observations of plasma wave characteristics in the auroral F region. *Annales Geophysicae*, 32(7), 875–888. <https://doi.org/10.5194/angeo-32-875-2014>
- Marholm, S., & Marchand, R. (2020). Finite-length effects on cylindrical Langmuir probes. *Physical Review Research*, 2, 023016. <https://doi.org/10.1103/PhysRevResearch.2.023016>
- Moen, J., Oksavik, K., Abe, T., Lester, M., Saito, Y., Bekkeng, T. A., & Jacobsen, K. S. (2012). First in-situ measurements of HF radar echoing targets. *Geophysical Research Letters*, 39(7). <https://doi.org/10.1029/2012GL051407>
- Moen, J., Oksavik, K., Alfonsi, L., Daabakk, Y., Romano, V., & Spogli, L. (2013). Space weather challenges of the polar cap ionosphere. *Journal of Space Weather and Space Climate*, 3, A02. <https://doi.org/10.1051/swsc/2013025>
- Moen, J., Walker, I. K., Kersley, L., & Milan, S. E. (2002). On the generation of cusp HF backscatter irregularities. *Journal of Geophysical Research*, 107(A4), SIA31–SIA35. <https://doi.org/10.1029/2001JA000111>
- Moser, C., LaBelle, J., Roglans, R., Bonnell, J. W., Cairns, I. H., Feltman, C., et al. (2021). Modulated upper-hybrid waves coincident with lower-hybrid waves in the cusp. *Journal of Geophysical Research: Space Physics*, 126(9), e2021JA029590. <https://doi.org/10.1029/2021JA029590>
- Oksavik, K. (2020a). *Documentation of GNSS total electron content and scintillation data (60 s) at Svalbard*. DataverseNO. <https://doi.org/10.18710/EA5BYX>
- Oksavik, K. (2020b). *The University of Bergen global navigation satellite system data collection*. DataverseNO. <https://doi.org/10.18710/AJ4S-X394>
- Oksavik, K., Moen, J., Lester, M., Bekkeng, T. A., & Bekkeng, J. K. (2012). In situ measurements of plasma irregularity growth in the cusp ionosphere. *Journal of Geophysical Research*, 117(A11), A11301. <https://doi.org/10.1029/2012JA017835>
- Pécseli, H. L. (2015). Spectral properties of electrostatic drift wave turbulence in the laboratory and the ionosphere. *Annales Geophysicae*, 33(7), 875–900. <https://doi.org/10.5194/angeo-33-875-2015>
- Pécseli, H. L., Primdahl, F., & Bahnsen, A. (1989). Low-frequency electrostatic turbulence in the polar cap E region. *Journal of Geophysical Research*, 94(A5), 5337–5349. <https://doi.org/10.1029/JA094iA05p05337>
- Pfaff, R. F., Jr., Mariotti, P. A., & Swartz, W. E. (1997). Wavevector observations of the two-stream instability in the daytime equatorial electrojet. *Geophysical Research Letters*, 24(13), 1671–1674. <https://doi.org/10.1029/97GL01535>
- Ponomarenko, P. V., & Waters, C. L. (2006). Spectral width of SuperDARN echoes: Measurement, use and physical interpretation. *Annales Geophysicae*, 24(1), 115–128. <https://doi.org/10.5194/angeo-24-115-2006>

- Ponomarenko, P. V., Waters, C. L., & Menk, F. W. (2007). Factors determining spectral width of HF echoes from high latitudes. *Annales Geophysicae*, 25(3), 675–687. <https://doi.org/10.5194/angeo-25-675-2007>
- Reiniusson, A., Stenberg, G., Norqvist, P., Eriksson, A. I., & Rönmark, K. (2006). Enhancement of electric and magnetic wave fields at density gradients. *Annales Geophysicae*, 24(1), 367–379. <https://doi.org/10.5194/angeo-24-367-2006>
- Ruohoniemi, J. M., Greenwald, R. A., Baker, K. B., Villain, J., Haniuise, C., & Kelly, J. (1989). Mapping high-latitude plasma convection with coherent HF radars. *Journal of Geophysical Research*, 94(A10), 13463–13477. <https://doi.org/10.1029/JA094iA10p13463>
- Ruohoniemi, J. M., Greenwald, R. A., Baker, K. B., Villain, J. P., & McCready, M. A. (1987). Drift motions of small-scale irregularities in the high-latitude F region: An experimental comparison with plasma drift motions. *Journal of Geophysical Research*, 92(A5), 4553–4564. <https://doi.org/10.1029/JA092iA05p04553>
- Sawyer, R. P., Fuselier, S. A., Kletzing, C. A., Bonnell, J. W., Roglans, R., Bounds, S. R., et al. (2021). TRICE 2 observations of low-energy magnetospheric ions within the cusp. *Journal of Geophysical Research: Space Physics*, 126(9), e2021JA029382. <https://doi.org/10.1029/2021JA029382>
- Seyler, C. E., Clark, A. E., Bonnell, J., & Wahlund, J.-E. (1998). Electrostatic broadband ELF wave emission by Alfvén wave breaking. *Journal of Geophysical Research*, 103(A4), 7027–7041. <https://doi.org/10.1029/97JA02297>
- Seyler, C. E., & Wahlund, J.-E. (1996). Theory of nearly perpendicular electrostatic plasma waves and comparison to Freja satellite observations. *Journal of Geophysical Research*, 101(A10), 21795–21813. <https://doi.org/10.1029/96JA02041>
- Spicher, A., Deshpande, K., Jin, Y., Oksavik, K., Zettergren, M. D., Clausen, L. B. N., et al. (2020). On the production of ionospheric irregularities via Kelvin-Helmholtz instability associated with cusp flow channels. *Journal of Geophysical Research: Space Physics*, 125(6), e2019JA027734. <https://doi.org/10.1029/2019JA027734>
- Spicher, A., Miloch, W. J., & Moen, J. I. (2014). Direct evidence of double-slope power spectra in the high-latitude ionospheric plasma. *Geophysical Research Letters*, 41(5), 1406–1412. <https://doi.org/10.1002/2014GL059214>
- Stasiewicz, K., & Gustafsson, G. (2000). Alfvén waves and structures: What can we learn with multipoint measurements on Cluster-II. In R. A. Harris (Ed.), (Vol. 449, p. 177). *Cluster-II workshop multiscale/multipoint plasma measurements*.
- Stasiewicz, K., & Khotyaintsev, Y. (2001). Reply to comment on “Identification of widespread turbulence of dispersive Alfvén waves”. *Geophysical Research Letters*, 28(7), 1405–1406. <https://doi.org/10.1029/2000GL012579>
- Stasiewicz, K., Khotyaintsev, Y., Berthomier, M., & Wahlund, J. E. (2000). Identification of widespread turbulence of dispersive Alfvén waves. *Geophysical Research Letters*, 27(2), 173–176. <https://doi.org/10.1029/1999GL010696>
- Streltsov, A. V., & Lotko, W. (2008). Coupling between density structures, electromagnetic waves and ionospheric feedback in the auroral zone. *Journal of Geophysical Research*, 113(A5), A05212. <https://doi.org/10.1029/2007JA012594>
- Tam, S. W. Y., Chang, T., Kintner, P. M., & Klatt, E. (2005). Intermittency analyses on the SIERRA measurements of the electric field fluctuations in the auroral zone. *Geophysical Research Letters*, 32(5), L05109. <https://doi.org/10.1029/2004GL021445>
- Temerin, M. (1978). The polarization, frequency, and wavelengths of high-latitude turbulence. *Journal of Geophysical Research*, 83(A6), 2609–2616. <https://doi.org/10.1029/JA083iA06p02609>
- Temerin, M. (1979). Doppler shift effects on double-probe-measured electric field power spectra. *Journal of Geophysical Research*, 84(A10), 5929–5934. <https://doi.org/10.1029/JA084iA10p05929>
- Temerin, M., & Kintner, P. M. (1989). Review of ionospheric turbulence. In *Plasma waves and instabilities at comets and in magnetospheres* (pp. 65–80). American Geophysical Union (AGU). <https://doi.org/10.1029/GM053p0065>
- Tennekes, E., Tennekes, H., Lumley, J., Lumley, J., & Technology, M. (1972). *A first course in turbulence*. M.I.T.Pr.
- Torrence, C., & Compo, G. P. (1998). A practical guide to wavelet analysis. *Bulletin of the American Meteorological Society*, 79(1), 61–78. [https://doi.org/10.1175/1520-0477\(1998\)079<0061:APGTWA>2.0.CO;2](https://doi.org/10.1175/1520-0477(1998)079<0061:APGTWA>2.0.CO;2)
- Tsinober, A. (2009). *An informal conceptual introduction to turbulence: Second edition of an informal introduction to turbulence*. Springer Netherlands. Retrieved from <https://books.google.no/books?id=HdC51CE5pUoC>
- Tsunoda, R. T. (1988). High-latitude F region irregularities: A review and synthesis. *Reviews of Geophysics*, 26(4), 719–760. <https://doi.org/10.1029/RG026i004p00719>
- Vallières, X., Villain, J. P., & André, R. (2003). Characterization of frequency effect in SuperDARN spectral width distributions. *Radio Science*, 38(1), 3-1–3-12. <https://doi.org/10.1029/2001RS002550>
- Van Dierendonck, A. J., Klobuchar, J., & Hua, Q. (1993). Ionospheric scintillation monitoring using commercial single frequency C/A code receivers. In *Proceedings of the 6th international technical meeting of the satellite division of the institute of navigation (ion gps 1993)* (pp. 1333–1342).
- Villain, J.-P., André, R., Pinnock, M., Greenwald, R. A., & Haniuise, C. (2002). A statistical study of the Doppler spectral width of high-latitude ionospheric F-region echoes recorded with SuperDARN coherent HF radars. *Annales Geophysicae*, 20(11), 1769–1781. <https://doi.org/10.5194/angeo-20-1769-2002>
- Villain, J. P., Caudal, G., & Haniuise, C. (1985). A Safari-Eiscat comparison between the velocity of F region small-scale irregularities and the ion drift. *Journal of Geophysical Research*, 90(A9), 8433–8443. <https://doi.org/10.1029/JA090iA09p08433>
- Vontrat-Reberac, A., Fontaine, D., Brelly, P.-L., & Galand, M. (2001). Theoretical predictions of the effect of cusp and dayside precipitation on the polar ionosphere. *Journal of Geophysical Research*, 106(A12), 28857–28865. <https://doi.org/10.1029/2001JA900131>
- Wahlund, J.-E., Eriksson, A. I., Holback, B., Boehm, M. H., Bonnell, J., Kintner, P. M., et al. (1998). Broadband ELF plasma emission during auroral energization: 1. Slow ion acoustic waves. *Journal of Geophysical Research*, 103(A3), 4343–4375. <https://doi.org/10.1029/97JA02008>
- Welch, P. (1967). The use of Fast Fourier transform for the estimation of power spectra: A method based on time averaging over short, modified periodograms. *IEEE Transactions on Audio and Electroacoustics*, 15(2), 70–73. <https://doi.org/10.1109/TAU.1967.1161901>
- Yeh, K. C., & Liu, C.-H. (1982). Radio wave scintillations in the ionosphere. *Proceedings of the IEEE*, 70(4), 324–360. <https://doi.org/10.1109/PROC.1982.12313>
- Yeoman, T. K., Chisham, G., Baddeley, L. J., Dhillon, R. S., Karhunen, T. J. T., Robinson, T. R., et al. (2008). Mapping ionospheric backscatter measured by the SuperDARN HF radars - Part 2: Assessing SuperDARN virtual height models. *Annales Geophysicae*, 26(4), 843–852. <https://doi.org/10.5194/angeo-26-843-2008>
- Yeoman, T. K., Wright, D. M., Engebretson, M. J., Lessard, M. R., Pilipenko, V. A., & Kim, H. (2012). Upstream-generated Pc3 ULF wave signatures observed near the Earth's cusp. *Journal of Geophysical Research*, 117(A3), A03202. <https://doi.org/10.1029/2011JA017327>